

# Nanoengineering of photonic crystal fibers for supercontinuum spectral shaping

Michael H. Frosz, Thorkild Sørensen, and Ole Bang

COM-DTU, Department of Communications, Optics and Materials, Technical University of Denmark,  
Ørsted's Plads 345V, DK-2800 Kongens Lyngby, Denmark

Received October 28, 2005; revised March 26, 2006; accepted April 7, 2006; posted April 19, 2006 (Doc. ID 65657)

Supercontinuum generation using picosecond pulses pumped into cobweb photonic crystal fibers is investigated. Dispersion profiles are calculated for several fiber designs and used to analytically investigate the influence of the fiber structural parameters (core size and wall thickness) on the location of the Stokes and anti-Stokes bands and gain bandwidth. An analysis shows that the Raman effect is responsible for reducing the four-wave mixing gain and a slight reduction in the corresponding frequency shift from the pump, when the frequency shift is much larger than the Raman shift. Using numerical simulations we find that four-wave mixing is the dominant physical mechanism for the pumping scheme considered, and that there is a trade-off between the spectral width and the spectral flatness of the supercontinuum. The balance of this trade-off is determined by nanometer-scale design of the fiber structural parameters. It is also shown that the relatively high loss of the nonlinear fiber does not significantly affect the supercontinuum generation. © 2006 Optical Society of America

OCIS codes: 060.2280, 190.4370, 190.5650.

## 1. INTRODUCTION

Pumping short pulses into a photonic crystal fiber (PCF) can generate an extremely broad, relatively flat optical spectrum, a so-called supercontinuum (SC). The SC is formed due to an interplay between several nonlinear optical effects in the PCF.<sup>1</sup> An SC source has many applications in, e.g., spectroscopy,<sup>2</sup> sensors,<sup>3</sup> and optical coherence tomography.<sup>4</sup> Two important advantages of using PCFs are the possibility of producing a small core, thus increasing the effective nonlinearity, and the possibility to precisely control the dispersion characteristics through the design of the PCF structure. The dispersion profile is essential, e.g., for the efficiency of parametric processes, such as four-wave mixing (FWM),<sup>5,6</sup> and for determining the wavelength at which dispersive waves are generated.<sup>7</sup> By controlling the dispersion of the PCF it is therefore also possible to partially shape the SC spectrum. Particularly in optical coherence tomography both the width and the smoothness of the spectrum are important for obtaining high image resolution.<sup>8</sup>

Previously, Apolonski *et al.* experimentally investigated femtosecond-pumped SC spectral shaping by varying the chirp, power, and polarization state of the input pulses, and by varying the core size of the PCF.<sup>9</sup> The possibility of optimizing the dispersion profile by choosing a proper core size was not fully explored, since only three different core sizes were used in the experiments. SC generation in fibers tapered to various degrees has been experimentally performed.<sup>10,11</sup> Again, the possibility of optimizing the dispersion profile for spectral shaping was not explored. Genty *et al.* used both experimental and numerical investigations to study how a femtosecond-pumped SC bandwidth can be enhanced by tailoring of the PCF dispersion profile.<sup>12</sup> Recently, we investigated SC generation by fem-

tosecond pumping in PCFs with two zero-dispersion wavelengths and different PCF structural parameters (corresponding to different dispersion profiles).<sup>7</sup> We have also investigated femtosecond-pumped SC generation in tapered fibers, where the dispersion profile varies along the tapered fiber length.<sup>13</sup> In both cases, it was found that control of the dispersion profile allows some degree of control over the resulting SC spectrum. For femtosecond pumping, the control of the SC spectrum is typically achieved by manipulating the soliton dynamics through dispersion engineering.<sup>7,12</sup> On the other hand, for picosecond pumping the SC spectrum can be modified by changing the phase-matching conditions determined by the dispersion profile,<sup>6</sup> which is also the study of this paper. Furthermore, since femtosecond pump lasers are typically complex systems, it is of great interest to study efficient SC generation using longer pulses, such as picoseconds or even nanoseconds, which can be produced by simpler lasers.<sup>5,14</sup>

Nikolov *et al.* showed that a picosecond-pumped SC could be generated more efficiently using proper dispersion design.<sup>6</sup> It was found that the spectrum becomes more flat if the dispersion profile ensures that the Stokes and anti-Stokes bands generated by partially degenerate FWM are sufficiently close to the pump, so that they can broaden themselves and merge with the pump into a flat continuum before losses and temporal splitting decrease the peak power to a level where nonlinear effects are no longer efficient. Furthermore, calculations showed that a broad FWM gain bandwidth makes the SC generation more robust against random variations of the PCF structure along the fiber length.<sup>6</sup> These calculations were based on experimental measurements of the dispersion profile variation over a 150 m span.<sup>15</sup> This means that

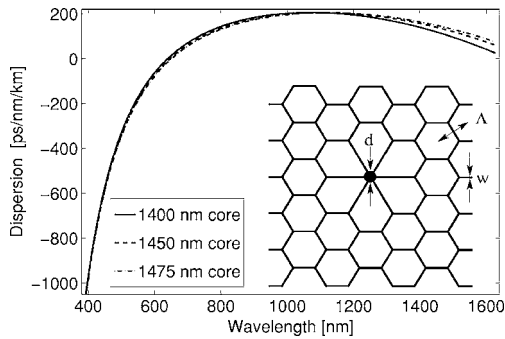


Fig. 1. Examples of three different dispersion curves, calculated for a cobweb structure (see inset) with wall thickness  $w = 130$  nm, pitch  $\Lambda = 8.53 \mu\text{m}$ , and core size  $d$  ranging from 1400 to 1475 nm.

fabrication tolerances can be expected to be less stringent for fibers designed so that the FWM gain bandwidth is broad.

In this paper, we determine to what degree the dispersion profile can be engineered by modifying the fiber structural parameters and to what extent this influences the SC spectrum. The investigation by Nikolov *et al.*<sup>6</sup> only considered dispersion profiles for a few particular PCF designs. In this paper, we make a detailed study of how the dispersion parameters vary as a function of the cobweb PCF core size and wall thickness. This includes an analysis showing how and why the maximum FWM bandwidth is obtained. We investigate how control of the core size and wall thickness can be used to modify the position of the Stokes and anti-Stokes bands and the FWM gain bandwidth, and how these FWM properties are affected by the Raman effect. It is thereby possible to shape the SC spectrum, and we examine whether there is an optimum core size and wall thickness. Shifting the Stokes and anti-Stokes bands away from the pump increases the width of the spectrum, but can introduce dips in the spectrum. We therefore also investigate how far away from the pump the Stokes and anti-Stokes bands can be moved before introducing dips in the spectrum. These investigations are done by numerical simulations of SC generation using picosecond pulses with 400 W peak power launched into a cobweb PCF<sup>16</sup> (see inset of Fig. 1 for an illustration of the fiber structure).

Our results show that changing the core size as little as 25 nm has a sufficient effect on the dispersion characteristics of the PCF to profoundly influence the picosecond-pumped SC generation. This is because even though the dispersion profile is changed only slightly, the effect on the phase-matching condition is significant. The simulations show that in the cases investigated here, the SC generation is mainly due to FWM. The SC is most efficiently generated when the Stokes and anti-Stokes bands are close enough to the pump for them to merge into a flat spectrum.<sup>6</sup> This occurs when the PCF is pumped in the anomalous dispersion region, close to the zero-dispersion wavelength. We show how the SC bandwidth and spectral flatness varies with (and is critically dependent on) core size and wall thickness. Finally, it is also found that a loss as high as 300 dB/km only slightly degrades the SC generation.

## 2. FOUR-WAVE MIXING THEORY

It is well known that SC generation using femtosecond pulses is typically (see, e.g., Refs. 7, 12, and 14) caused by self-phase modulation (SPM), fission of higher-order solitons followed by soliton self-frequency shift, and amplification of dispersive waves. For picosecond pulse pumping, SPM is typically less dominant since the SPM spectral broadening is inversely proportional to the temporal width of the pulses.<sup>17</sup> Instead, it is known that the spectral broadening is mainly caused by FWM and stimulated Raman scattering.<sup>5,6,18,19</sup> As will be shown in subsection 3.C, FWM is also the dominant SC mechanism in the cases investigated here.

FWM can be viewed as the process where two photons with angular frequencies  $\omega_1$  and  $\omega_2$  are annihilated while creating two new photons with frequencies  $\omega_3$  and  $\omega_4$ .<sup>17</sup> If  $\omega_1 = \omega_2$  the process is called partially degenerate FWM, and  $\omega_1 = \omega_0$ ,  $\omega_3 = \omega_S < \omega_0$ , and  $\omega_4 = \omega_{aS} > \omega_0$  are called the pump, Stokes, and anti-Stokes frequencies, respectively.

To fully clarify the influence of both the Raman effect and of higher-order dispersion on FWM, we generalize the theory presented in Ref. 17, as was also done by Shuang-Chun *et al.*<sup>20</sup> The generalized nonlinear Schrödinger equation is used in the numerical simulations and shown in subsection 3.C. For the analysis in this section, we neglect the self-steepening term and losses. We then have<sup>17,20</sup>

$$\frac{\partial A}{\partial z} = i \sum_{m \geq 2} \frac{i^m \bar{\beta}_m}{m!} \frac{\partial^m A}{\partial T^m} + i \gamma A(z, T) \int_{-\infty}^{\infty} R(T') |A(z, T - T')|^2 dT', \quad (1)$$

where  $A(z, T)$  is the pulse envelope in a retarded time frame  $T = t - \bar{\beta}_1 z$  moving with the group velocity  $1/\bar{\beta}_1$  of the pump, along the fiber axis  $z$ .  $\gamma = n_2 \omega_0 / [c A_{\text{eff}}]$  is the nonlinear parameter, where  $n_2 = 2.6 \times 10^{-20} \text{ m}^2/\text{W}$  is the nonlinear index coefficient for silica;  $c$  is the speed of light in vacuum; and  $A_{\text{eff}}$  is the effective core area.<sup>17</sup> In this paper we approximate the effective area with the core area,  $A_{\text{eff}} \approx A_{\text{core}}$ . The frequency dependence of  $A_{\text{eff}}$  is small and therefore neglected.  $P_0$  is the peak power of the pump pulse, and  $\bar{\beta}_m$  are the dispersion parameters defined as<sup>17</sup>

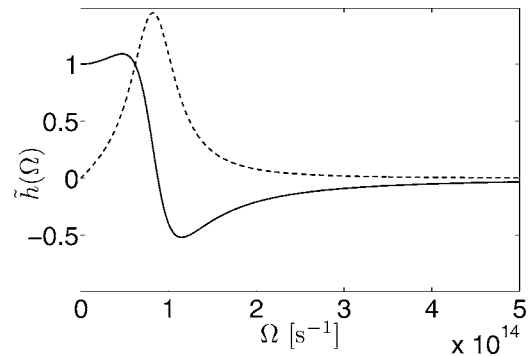


Fig. 2. Real (solid curve) and imaginary (dashed curve) part of  $\hat{h}(\Omega)$ , as given by Eq. (7). The peak of the imaginary part occurs at  $\Omega = \Omega_R = 2\pi \times 13.2 \text{ THz}$ .

$$\bar{\beta}_m = \beta_m(\omega_0) = \left( \frac{d^m \beta}{d\omega^m} \right)_{\omega=\omega_0}, \quad (2)$$

where  $\beta = \beta(\omega)$  is the mode propagation constant.  $R(t)$  is the Raman response function<sup>17,21</sup>

$$R(t) = (1 - f_R)\delta(t) + f_R h(t) = (1 - f_R)\delta(t) + f_R \frac{\tau_1^2 + \tau_2^2}{\tau_1 \tau_2} \times \exp(-t/\tau_2) \sin(t/\tau_1) \Theta(t), \quad (3)$$

where  $f_R = 0.18$  is the fractional contribution of the delayed Raman response,  $\tau_1 = 12.2$  fs, and  $\tau_2 = 32$  fs.  $\Theta(t)$  is the Heaviside step function.

Performing a similar linear stability analysis as in Refs. 17 and 20 for a perturbation of the form

$$a(z, T) = a_1 \exp[i(Kz - \Omega T)] + a_2 \exp[-i(Kz - \Omega T)], \quad (4)$$

we arrive at the dispersion relation

$$K = \sum_{m=1}^{\infty} \frac{\beta_{2m+1}}{(2m+1)!} \Omega^{2m+1} \pm \sqrt{\sum_{m=1}^{\infty} \frac{\beta_{2m}}{(2m)!} \Omega^{2m} + 2\gamma P_0(1 - f_R + f_R \tilde{h})} \left[ \sum_{m=1}^{\infty} \frac{\beta_{2m}}{(2m)!} \Omega^{2m} \right], \quad (5)$$

where  $\tilde{h}$  is the Fourier transform of  $h(t)$  appearing in Eq. (3), given by

$$\tilde{h}(\Omega) = \frac{\tau_1^2 + \tau_2^2}{\tau_2^2 - \tau_1^2(i + \tau_2 \Omega)^2}. \quad (6)$$

We now consider the situation where the Stokes and anti-Stokes frequencies are far away from the peak of the Raman gain at 13.2 THz:  $\Omega = \omega_0 - \omega_S = \omega_{aS} - \omega_0 \gg 2\pi \times 13.2$  THz. In this case,  $\tilde{h}(\omega) \approx 0$ , as can be seen from Fig. 2, and the parametric gain  $g = \text{Im}(K)$  of the perturbation is

$$g(\Omega) = \sqrt{-\left[ \sum_{m=1}^{\infty} \frac{\beta_{2m}}{(2m)!} \Omega^{2m} + 2\gamma P_0(1 - f_R) \right] \sum_{m=1}^{\infty} \frac{\beta_{2m}}{(2m)!} \Omega^{2m}}, \quad \Omega \gg \Omega_R, \quad (7)$$

where  $\Omega_R = 2\pi \times 13.2$  THz.

From this it is found that the maximum gain occurs for frequency shifts  $\Omega_0$  satisfying

$$\sum_{m=1}^{\infty} \frac{\beta_{2m}}{(2m)!} \Omega_0^{2m} = -\gamma P_0(1 - f_R), \quad \Omega \gg \Omega_R. \quad (8)$$

The gain can also be written as

$$g(\Omega) = \sqrt{[\gamma P_0(1 - f_R)]^2 - (\kappa/2)^2}, \quad \Omega \gg \Omega_R, \quad (9)$$

where  $\kappa$  is the phase mismatch given by

$$\kappa = 2\gamma P_0(1 - f_R) + 2 \sum_{m=1}^{\infty} \frac{\beta_{2m}}{(2m)!} \Omega^{2m}, \quad \Omega \gg \Omega_R. \quad (10)$$

The influence of FWM on the Raman effect is well known,<sup>22,23</sup> but Eqs. (9) and (10) show the influence of the Raman effect on FWM. To the best of our knowledge, it has not previously been directly shown that the  $(1 - f_R)$  factor appears when  $\Omega \gg \Omega_R$ . We elaborate further on the consequences of this factor in Subsection 3.D.

Partially degenerate FWM requires that the energy conservation condition  $2\omega_0 = \omega_S + \omega_{aS}$  is fulfilled, but also that the three waves are phase matched according to Eq. (10), where  $\Omega = \omega_0 - \omega_S = \omega_{aS} - \omega_0$  is the angular frequency shift from the pump in the FWM process. A detailed investigation of the relation between FWM and higher-order dispersion has been made by Biancalana *et al.*<sup>24</sup>

From Eq. (9) it is seen that there is a gain for FWM if  $|\kappa| < 2\gamma P_0(1 - f_R)$ . This means that partially degenerate

FWM will transfer energy from the pump to all the wavelengths for which this condition is fulfilled.

We have calculated the phase mismatch  $\kappa$  and the gain  $g$  for three different core sizes in Fig. 3 (the calculation of

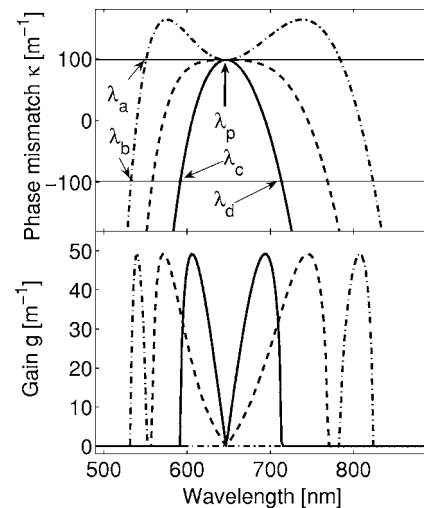


Fig. 3. Top: Phase mismatch  $\kappa$  for cobweb PCFs with  $\Lambda = 8.53$   $\mu\text{m}$ ,  $w = 130$  nm, and  $d = 1400$  nm (solid curve), 1450 nm (dashed curve), and 1475 nm (dashed-dotted curve); the pump wavelength is 647 nm,  $\gamma = 0.15$   $(\text{Wm})^{-1}$  (the slight variation of  $\gamma$  with core size is neglected in this figure), and  $P_0 = 400$  W. The upper and lower horizontal lines at  $\kappa = \pm 2\gamma P_0(1 - f_R) = \pm 98.4$   $\text{m}^{-1}$  indicate the borders of the gain region. For  $d = 1400$  nm,  $\beta_2 < 0$ ; for  $d = 1450$  nm,  $\beta_2 \approx 0$ ; and for  $d = 1475$  nm,  $\beta_2 > 0$ . Bottom: Corresponding parametric gain given by Eq. (9).

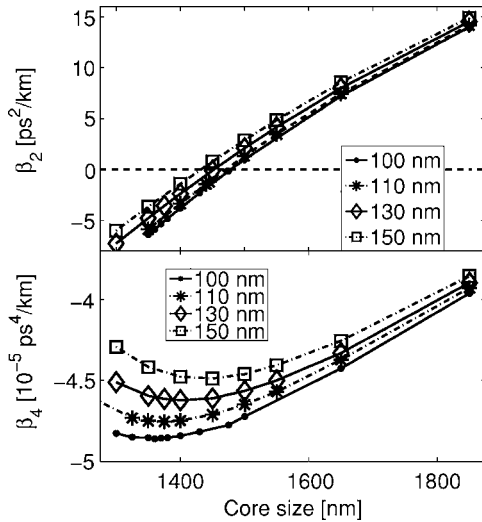


Fig. 4. Dispersion parameters  $\bar{\beta}_2$  (top) and  $\bar{\beta}_4$  (bottom) calculated for a wide range of two of the cobweb-fiber structural parameters: core size  $d$  and wall thickness  $w$  are given in the inset.

the dispersion parameters is explained in Subsection 3.A). For the three selected fiber designs we have  $\bar{\beta}_2 < 0$ ,  $\bar{\beta}_2 \approx 0$ , and  $\bar{\beta}_2 > 0$  for the  $d=1400, 1450$ , and  $1475$  nm fibers, respectively. For the  $d=1400$  nm fiber, the Stokes gain bandwidth in Fig. 3 is  $\lambda_d - \lambda_p$ , and the anti-Stokes gain bandwidth is  $\lambda_p - \lambda_c$  (see Fig. 3). The Stokes gain region is thus directly connected to the anti-Stokes gain region at  $\lambda_p$ . When  $\bar{\beta}_2$  is increased to almost zero, as for the  $d=1450$  nm core fiber, the Stokes and anti-Stokes peaks (the wavelengths for which the gain  $g$  is maximum, at  $\kappa=0$ ) shift away from the pump and their gain bandwidths increase. However, as soon as  $\bar{\beta}_2$  becomes positive, as for the  $d=1475$  nm core fiber, the Stokes and anti-Stokes bands separate and their gain bandwidths decrease. In Fig. 3 the anti-Stokes gain bandwidth in this case is  $\lambda_a - \lambda_b$  and there is no energy transfer to wavelengths between  $\lambda_a$  and  $\lambda_p$  from partially degenerate FWM. Similarly, the Stokes band will be separated from the pump by a region without gain. From Fig. 3 we therefore expect that PCFs where  $\bar{\beta}_2$  is positive will lead to a broad spectrum, but possibly with a discontinuity between the pump and the Stokes and anti-Stokes spectral bands. As shown in Subsection 3.C this can occur if the fiber is too short.

On the other hand, for fibers with a small but negative  $\bar{\beta}_2$ , there is a FWM gain for a broad continuous range of wavelengths from the pump to the immediately adjacent Stokes and anti-Stokes gain regions. This should therefore result in a smoother spectrum.

It is usually recommended to pump in the anomalous dispersion regime, close to the zero-dispersion wavelength (corresponding to a small, negative  $\bar{\beta}_2$ ), to obtain phase matching for FWM.<sup>17</sup> In our case, we note that since  $\bar{\beta}_4 < 0$  (shown in Section 3), phase matching can also occur when pumping in the normal dispersion regime. However, we still expect an advantage of anomalous pumping, because we know from Fig. 3 that this should result in a smoother spectrum.

### 3. NUMERICAL RESULTS

#### A. Dispersion Curves

We have calculated several dispersion curves for varying core size  $d$  and wall thickness  $w$  in the cobweb PCF structure using a semivectorial finite-difference method.<sup>25,26</sup> The calculation time for each fiber structure was approximately 12–24 h on a PC with a 2.9 GHz processor and 4.5 Gbytes RAM. Examples of three different dispersion profiles are given in Fig. 1, for fixed pitch  $\Lambda=8.53$   $\mu\text{m}$  and wall thickness  $w=130$  nm.

By fitting the calculated  $\beta_2$  dispersion profile [ $\beta_2(\omega) = -2\pi cD/\omega^2$ , where  $D$  is the dispersion parameter<sup>17</sup> and  $c$  is the speed of light in vacuum] to a polynomial of the form

$$\beta_2(\omega) = \bar{\beta}_2 + \bar{\beta}_3[\omega - \omega_0] + \frac{1}{2}\bar{\beta}_4[\omega - \omega_0]^2 + \frac{1}{6}\bar{\beta}_5[\omega - \omega_0]^3 + \dots \quad (11)$$

$$\approx b_2 + b_3[\omega - \omega_0] + \dots + \frac{1}{(M-2)!}b_M[\omega - \omega_0]^M, \quad (12)$$

we extract the parameters  $b_2, \dots, b_M$ . This is because it is difficult to accurately calculate the higher-order derivatives necessary in Eq. (2) from the numerical data. We found that using  $M=14$  ensured a good polynomial fit to the dispersion curves over the entire wavelength range of interest. Note that since each  $b_m$  coefficient is obtained from a least-squares polynomial fit, they do not necessarily correspond to the  $\bar{\beta}_m$  coefficients as defined in Eq. (2). This distinction is often neglected in the literature, where polynomial fits to dispersion curves are widely used (see, e.g., Refs. 5 and 14).

It can easily be shown that if

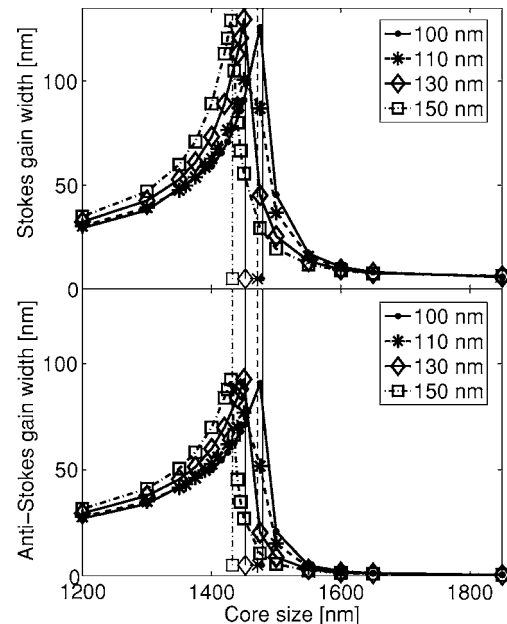


Fig. 5. Stokes (top) and anti-Stokes (bottom) gain bandwidth as a function of core size  $d$  and wall thickness  $w$ . The vertical lines indicate the core size at which  $\bar{\beta}_2=0$  for the various wall thicknesses.

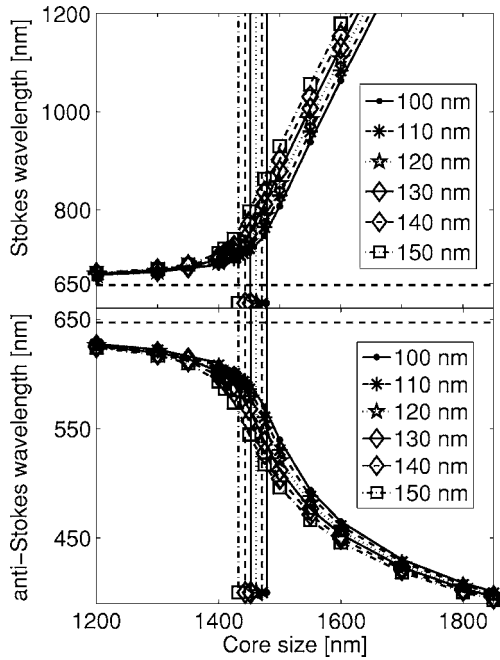


Fig. 6. Stokes (top) and anti-Stokes (bottom) wavelengths for various values of the core size  $d$  and the wall thickness  $w$ . The vertical lines indicate the core size at which  $\bar{\beta}_2=0$  for the various wall thicknesses. The dashed horizontal lines indicate the pump wavelength.

$$b(\omega) = b_0 + b_1[\omega - \omega_0] + \frac{1}{2}b_2[\omega - \omega_0]^2 + \dots + \frac{1}{M!}b_M[\omega - \omega_0]^M \quad (13)$$

is a good fit to  $\beta(\omega)$ , then Eq. (10) is still valid when replacing the  $\bar{\beta}$  coefficients with the  $b$  coefficients. To avoid confusion, we will therefore in the following write  $\bar{\beta}_m$ , even though we, strictly speaking, mean the least-squares-fitted  $b_m$  coefficient.

### B. Four-Wave Mixing Parameters

As seen in Fig. 4, we found that  $\bar{\beta}_2$  can be significantly modified by varying the core size  $d$  and/or the wall thickness  $w$ . We also found that the fourth-order dispersion parameter  $\bar{\beta}_4$  is almost constant at around  $-4 \times 10^{-5} \text{ ps}^4/\text{km}$  when varying  $d$  and  $w$  within the parameter space investigated here. As seen from Eq. (10), a non-zero  $\bar{\beta}_4$  is therefore expected to limit the FWM gain bandwidth when  $\bar{\beta}_2=0$ .

The important thing to note from Fig. 4 is that, although one cannot obtain a dispersion profile with zero curvature ( $\bar{\beta}_4 \approx 0$ ), note that the slope of the dispersion profile,  $\bar{\beta}_3$ , is unimportant for the phase-matching condition) within the parameter range investigated here, it is still possible to tune  $\bar{\beta}_2$  in the range  $-5$  to  $15 \text{ ps}^2/\text{km}$  through selection of core size and/or wall thickness. This means that we can significantly change the phase mismatch plot, as indicated in Fig. 3, and thereby control the wavelength range at which new frequencies are generated. The Stokes and anti-Stokes gain bandwidths are plotted for various fiber designs in Fig. 5, and defined in Fig. 3 as the regions where  $|\kappa| < 2\gamma P_0(1-f_R)$ . The anti-

Stokes gain bandwidth in Fig. 3, e.g., is  $\lambda_a - \lambda_b$  for the  $d = 1475 \text{ nm}$  fiber, and  $\lambda_p - \lambda_c$  for the  $d = 1400 \text{ nm}$  fiber.

It is seen from Fig. 5 how the Stokes and anti-Stokes gain bandwidths increase as the core size is increased, until dropping rapidly after the core size where  $\bar{\beta}_2=0$  (indicated by the vertical lines). This is understood graphically from Fig. 3 by noting the behavior of the phase mismatch plot when  $\bar{\beta}_2$  goes from below to above zero.

The Stokes and anti-Stokes wavelengths for several fiber designs are plotted in Fig. 6. The Stokes and anti-Stokes wavelengths are the wavelengths at which  $\kappa=0$  and there is therefore maximum gain at these wavelengths, see Eq. (9). It is seen that the more the core size and/or the wall thickness is increased, the further away the Stokes and anti-Stokes lines shift from the pump. However, we know from Fig. 5 that the gain bandwidth becomes narrow when the core size and wall thickness is large enough for  $\bar{\beta}_2$  to become positive. As seen in Subsection 3.C, a small gain bandwidth leads to spectral dips in the SC. Furthermore, the SC generation is less robust to PCF structural variations (e.g., core size and wall thickness) along the fiber length if the gain bandwidth is small.<sup>6</sup> Therefore there is a trade-off between the flatness and the width of the SC spectrum.

### C. Calculated Spectra

To evaluate the usefulness of the various fiber designs in SC generation, we have simulated pulse propagation in the fibers using the generalized nonlinear Schrödinger equation<sup>17</sup>:

$$\frac{\partial A}{\partial z} = i \sum_{m \geq 2} \frac{i^m \bar{\beta}_m}{m!} \frac{\partial^m A}{\partial T^m} - \frac{\alpha}{2} A + i\gamma \left[ 1 + \frac{i}{\omega_0} \frac{\partial}{\partial T} \right] \times \left[ A(z, T) \int_{-\infty}^{\infty} R(T') |A(z, T - T')|^2 dT' \right]. \quad (14)$$

$\alpha$  is the attenuation coefficient, which we assume to be

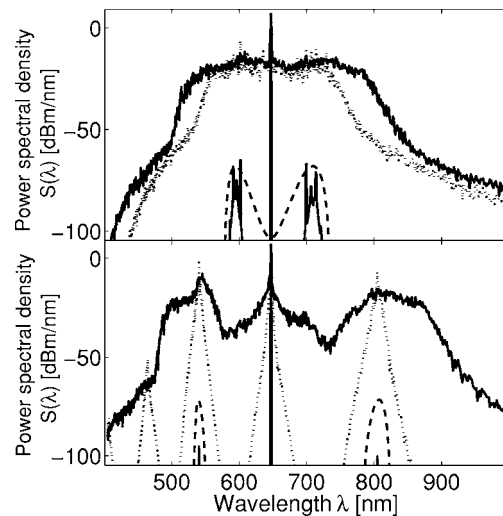


Fig. 7. Calculated spectra for  $d=1425 \text{ nm}$  core (top),  $1475 \text{ nm}$  core (bottom) and  $w=130 \text{ nm}$ , at  $z=0.6 \text{ m}$  (solid, lowest curve),  $z=0.9 \text{ m}$  (dotted curve), and  $z=1.2 \text{ m}$  (solid, highest curve). The parametric gain  $g$  is included (dashed curves) in arbitrary units to show how well the locations of the Stokes and anti-Stokes bands are predicted.

wavelength independent; the loss is set to 300 dB/km, which is realistic for a cobweb fiber with the core sizes modeled here.<sup>27</sup> For simplification, we also assume that the fiber is polarization maintaining and pumped along one polarization axis.

Again, as in Subsection 3.A, we note that even though Eq. (14) contains the  $\bar{\beta}_m$  coefficients, we can use the least-squares-fitted  $b_m$  coefficients instead if the number of fitting coefficients  $M$  is large enough.

The propagation equation is solved using the well-known split-step Fourier method,<sup>17</sup> implemented using the adaptive step-size method outlined by Sinkin *et al.*,<sup>28</sup> since it reduces the total number of Fourier transforms and thus increases computation speed. We have used  $N=2^{17}$  points and a temporal resolution of 1.8 fs, giving a time window of 236 ps. The local goal error used in the adaptive step-size method was set to  $\delta_G=10^{-7}$ . This resulted in a step size of typically 1–4  $\mu\text{m}$ . We first performed the calculations without loss. The relative change in the total photon number  $P$ , a measure of the numerical error that is ideally zero in the absence of loss,<sup>21</sup> was less than 2.5%. The photon number  $P$  is calculated as<sup>21</sup>

$$P(z) = \int \frac{|\tilde{A}(z, \omega)|^2}{\omega} d\omega, \quad (15)$$

and the requirement of photon number conservation can be stated as  $\partial P/\partial z=0$ .  $\tilde{A}(z, \omega)$  is the Fourier transform of  $A(z, t)$ . We then repeated the calculations, but included the 300 dB/km wavelength-independent loss. The simulation time for propagation in 1.2 m of fiber varied between 11 days ( $d=1425$  nm,  $w=130$  nm) and 31 days ( $d=1475$  nm,  $w=130$  nm) on a 2.2 GHz standard PC. The simulation time depends on the structural parameters because modulation instability accompanied by the FWM leads to temporal fluctuations in the time domain of the pulse. The further away the Stokes and anti-Stokes bands are located from the pump, the faster the temporal fluctuations.<sup>17</sup> The faster the pulse fluctuates in the time domain, the shorter the step size has to be so as to keep the numerical error of each step below the local goal error. This is done automatically by the adaptive step-size method.

The pump pulse parameters are center wavelength  $\lambda_0=647$  nm, pulse intensity full width at half-maximum  $T_{\text{FWHM}}=30$  ps, and peak power  $P_0=400$  W. The power spectral densities  $S(\lambda)$ ,

$$S(\lambda) = \frac{c}{\lambda^2} S(\nu) = \frac{c}{\lambda^2} f_{\text{rep}} |\tilde{A}(\nu)|^2, \quad (16)$$

where  $\nu=\omega/(2\pi)$ , presented here are normalized so that  $\int S(\lambda) d\lambda = P_{\text{av}}$ , where  $P_{\text{av}}=P_0 \sqrt{\pi} T_0 f_{\text{rep}}$  is the average pulse power of the Gaussian-shaped input pulse.  $T_0=T_{\text{FWHM}}/1.665$  and the repetition rate  $f_{\text{rep}}=590$  kHz. Similar pump parameters were used in the theoretical investigation by Nikolov *et al.*<sup>6</sup> and in the experiments by Coen *et al.*,<sup>5</sup> so these are physically realistic parameters.

The spectra presented in this paper have been smoothed over 128 points, resulting in a frequency resolution of  $\Delta\nu=128/(\Delta T)\approx 0.5$  THz, corresponding to ap-

proximately 0.8 nm in the vicinity of the pump wavelength 647 nm.  $\Delta T=236$  ps is the temporal width of the calculation domain.

Figure 7 shows the evolution of the calculated spectra along the fiber length for two different core sizes. It is clearly seen how a larger core size results in Stokes and anti-Stokes bands further away from the pump. Furthermore, the location of the Stokes and anti-Stokes bands is seen to agree excellently with Fig. 6 and the gain bands shown in Fig. 7. We also note that for a core size of  $d=1425$  nm, the Stokes and anti-Stokes bands are already merged with the pump at  $z=0.9$  m, and a smooth broad continuum is formed. For a core size of  $d=1475$  nm, the merging is first observed at  $z=1.2$  m. Even at this fiber length, the merging has not been as efficient as for the smaller core, and therefore spectral dips occur between the pump and the Stokes and anti-Stokes bands. It is possible that further propagation in a longer fiber would lead to further merging and a decrease of the spectral dips, but this was not investigated since the simulations are quite time-consuming. Furthermore, the bandwidth of the spectrum continuously increases along the fiber, and the propagation Eq. (14) is valid only for forward-traveling waves with a bandwidth less than  $\approx 1/3$  of  $\omega_0=2\pi c/\lambda_0$ .<sup>21</sup> We are already within this limit after 1.2 m of propagation.

Figure 8 compares the calculated spectra after 1.2 m of propagation in three different fiber designs, all with a wall thickness of  $w=130$  nm. From Fig. 4 we know that  $\bar{\beta}_2$  changes sign at a core size of approximately 1450 nm. As is also seen from Fig. 5, we therefore expect spectral dips to appear between the pump and the Stokes and anti-Stokes bands in the SC when the core size exceeds 1450 nm (for a fiber with  $w=130$  nm). This is also what we observe in Fig. 8: Increasing the core size from 1450 to 1475 nm widens the spectrum, but introduces a spectral dip between the pump and the Stokes and anti-Stokes lines. This demonstrates the important role of accurate fiber design to optimize the dispersion profile to obtain a flat SC.

Finally, in Fig. 9 we have compared two simulations with and without the wavelength-independent loss of 300 dB/km. For a fiber length of 1.2 m, the linear loss is only 0.36 dB. Nevertheless, the nonlinear effects could be highly sensitive to even a small loss, which is therefore

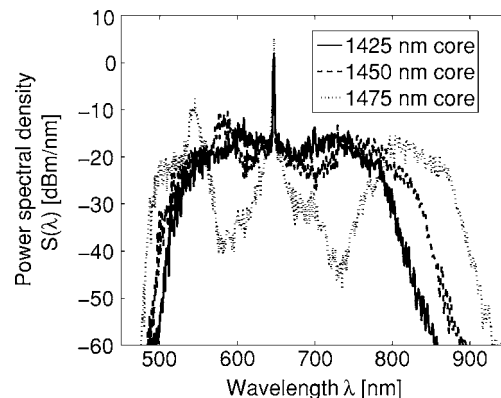


Fig. 8. Calculated output spectra after 1.2 m of propagation in three different fibers. The wall thickness  $w=130$  nm.

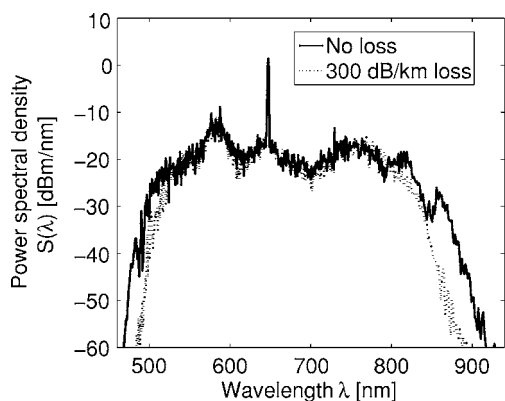


Fig. 9. Calculated output spectra after 1.2 m of propagation in the  $d=1450$  nm,  $w=130$  nm fiber, without loss in the simulation (solid curve) and including a wavelength-independent loss of 300 dB/km (dotted curve).

investigated. It is seen in Fig. 9 that including the loss does not significantly affect the central part of the SC spectrum, and only slightly reduces the width of the spectrum. In the cases investigated here, it is therefore seen that the relatively high losses of the nonlinear PCF do not have a significant effect on the SC generation.

#### D. Discussion of Physical Mechanisms

As mentioned above, there is an excellent agreement between the location of the Stokes and anti-Stokes bands calculated in Fig. 6 and the location of the Stokes and anti-Stokes peaks in the simulated spectra in Fig. 7. The peaks merge due to cross-phase modulation (XPM), and the degree of merging with the pump is determined by the distance between the pump wavelength and the Stokes and anti-Stokes bands. The resulting spectra can thus be explained physically solely on the basis of FWM and XPM.

The influence of the Raman effect is clearly seen from the equations in Section 2. From Eq. (9), the maximum gain obtained for  $\kappa=0$  is

$$g_{\max} = 2\gamma P_0(1 - f_R), \quad \Omega \gg \Omega_R, \quad (17)$$

which means that the Raman effect is responsible for reducing the FWM gain by a factor of  $(1 - f_R)$ . We have confirmed this by making simulations where  $f_R$  was set to zero, and observed a more rapid growth of the Stokes and anti-Stokes peaks than with  $f_R=0.18$ .

The Raman effect is also responsible for shifting the location of the Stokes and anti-Stokes peaks. From Eq. (8), we find for the case where all higher-order dispersion terms are negligible:

$$\Omega_{\max}^2 = \frac{-2\gamma P_0(1 - f_R)}{\beta_2}, \quad \Omega \gg \Omega_R. \quad (18)$$

In this case,  $\Omega_{\max}$  is reduced by a factor of  $\sqrt{(1 - f_R)}$ , corresponding to a shift of  $\approx 10\%$ . For the case where  $\beta_2$  is negligible (close to the zero-dispersion wavelength) and dispersion terms higher than  $\beta_4$  are neglected, we obtain

$$\Omega_{\max}^4 = \frac{-24\gamma P_0(1 - f_R)}{\beta_4}, \quad \Omega \gg \Omega_R, \quad (19)$$

which means that in this case the Raman effect only results in a peak shift of  $1 - (1 - f_R)^{1/4} \approx 5\%$ .

At the beginning of the fiber, the Raman effect is therefore responsible for reducing the growth rate of the FWM peaks, and slightly shifting the location of the peaks. For longer fibers we expect that the pulse will eventually break up into femtosecond solitons due to the modulation instability (see, e.g., Ref. 29). The Raman effect then causes the solitons to redshift (soliton self-frequency shift).<sup>17</sup>

## 4. CONCLUSIONS

It has been demonstrated how the design of a cobweb photonic crystal fiber affects supercontinuum generation using picosecond pulses. It was found that there is an inherent trade-off between the width of the spectrum (determined by the location of the Stokes and anti-Stokes bands) and the flatness of the spectrum. The spectrum is relatively flat when there is a continuous gain region between the pump and the Stokes and anti-Stokes lines. This occurs for fibers where  $\bar{\beta}_2 < 0$  (pumping in the anomalous dispersion region), and can be achieved by appropriate fiber design. Calculations of pulse propagation in the fibers demonstrated how an increase in core size of only 25 nm significantly affects the resulting spectrum, by widening the spectrum but at the same time degrading the flatness of the spectrum.

For comparison, random variations of the core size along the fiber length arising during fabrication are typically less than 1% over hundreds of meters of fiber.<sup>30</sup> Measurements show that the outer diameter of a 125  $\mu\text{m}$  fiber varies less than  $\pm 0.5$   $\mu\text{m}$  over such long fiber lengths. Assuming that the core size scales with the outer diameter, this corresponds to a variation in core size of less than  $\pm 5.6$  nm for a 1400 nm core size. For shorter fiber lengths, such as the ones modeled here, the variation in core size can be expected to be significantly less.<sup>30</sup> An increase in core size of 25 nm can therefore not be expected to occur due to random variations along the fiber length, and the supercontinuum generation should therefore be robust against such fiber irregularities.

A generalization of the standard four-wave mixing theory<sup>17</sup> showed that the Raman effect is responsible for reducing the four-wave mixing gain, and for slightly shifting the Stokes and anti-Stokes peaks closer to the pump, in the case where the peaks are much further away from the pump than the Raman shift of 13.2 THz in silica.

It was also shown that the relatively high loss of the cobweb photonic crystal fiber does not significantly affect the supercontinuum generation.

## ACKNOWLEDGMENTS

The authors thank Jesper Riishede and Jesper Lægsgaard for their helpful support and discussions on calculating the dispersion profiles. The authors also thank Kim

P. Hansen, Crystal Fiber A/S, for helpful information about the variations in fiber geometry along the fiber length.

The e-mail address for M. H. Frosz is [mf@com.dtu.dk](mailto:mf@com.dtu.dk).

## REFERENCES

- R. R. Alfano, ed., *The Supercontinuum Laser Source* (Springer-Verlag, 1989).
- A. Freiberg, J. A. Jackson, S. Lin, and N. W. Woodbury, "Subpicosecond pump-supercontinuum probe spectroscopy of LH2 photosynthetic antenna," *J. Phys. Chem. A* **102**, 4372–4380 (1998).
- P. V. Kelkar, F. Coppinger, A. S. Bhusan, and B. Jalali, "Time-domain optical sensing," *Electron. Lett.* **35**, 1661–1662 (1999).
- I. Hartl, X. D. Li, C. Chudoba, R. K. Ghanta, T. H. Ko, J. G. Fujimoto, J. K. Ranka, and R. S. Windeler, "Ultra-high-resolution optical coherence tomography using continuum generation in an air-silica microstructure optical fiber," *Opt. Lett.* **26**, 608–610 (2001).
- S. Coen, A. H. L. Chau, R. Leonhardt, J. D. Harvey, J. C. Knight, W. J. Wadsworth, and P. St. J. Russell, "Supercontinuum generation by stimulated Raman scattering and parametric four-wave mixing in photonic crystal fibers," *J. Opt. Soc. Am. B* **19**, 753–764 (2002).
- N. I. Nikolov, T. Sørensen, O. Bang, and A. Bjarklev, "Improving efficiency of supercontinuum generation in photonic crystal fibers by direct degenerate four-wave mixing," *J. Opt. Soc. Am. B* **20**, 2329–2337 (2003).
- M. H. Frosz, P. Falk, and O. Bang, "The role of the second zero-dispersion wavelength in generation of supercontinua and bright-bright soliton-pairs across the zero-dispersion wavelength," *Opt. Express* **13**, 6181–6192 (2005).
- A. F. Fercher, W. Drexler, C. K. Hitzenberger, and T. Lasser, "Optical coherence tomography—principles and applications," *Rep. Prog. Phys.* **66**, 239–303 (2003).
- A. Apolonski, B. Povazay, A. Unterhuber, W. Drexler, W. J. Wadsworth, J. C. Knight, and P. St. J. Russell, "Spectral shaping of supercontinuum in a cobweb photonic-crystal fiber with sub-20-fs pulses," *J. Opt. Soc. Am. B* **19**, 2165–2170 (2002).
- T. A. Birks, W. J. Wadsworth, and P. St. J. Russell, "Supercontinuum generation in tapered fibers," *Opt. Lett.* **25**, 1415–1417 (2000).
- S. G. Leon-Saval, T. A. Birks, W. J. Wadsworth, P. St. J. Russell, and M. W. Mason, "Supercontinuum generation in submicron fibre waveguides," *Opt. Express* **12**, 2864–2869 (2004).
- G. Genty, M. Lehtonen, H. Ludvigsen, and M. Kaivola, "Enhanced bandwidth of supercontinuum generated in microstructured fibers," *Opt. Express* **12**, 3471–3480 (2004).
- P. Falk, M. H. Frosz, and O. Bang, "Supercontinuum generation in a photonic crystal fiber with two zero-dispersion wavelengths tapered to normal dispersion at all wavelengths," *Opt. Express* **13**, 7535–7545 (2005).
- J. M. Dudley, L. Provino, N. Grossard, H. Maillotte, R. S. Windeler, B. J. Eggleton, and S. Coen, "Supercontinuum generation in air-silica microstructured fibers with nanosecond and femtosecond pulse pumping," *J. Opt. Soc. Am. B* **19**, 765–771 (2002).
- K. P. Hansen, J. R. Jensen, C. Jacobsen, H. R. Simonsen, J. Broeng, P. M. W. Skovgaard, A. Petersson, and A. Bjarklev, "Highly nonlinear photonic crystal fiber with zero-dispersion at 1.55  $\mu\text{m}$ ," in *Optical Fiber Communication Conference* (Optical Society of America, 2002), pp. FA91–FA93.
- M. H. Frosz, T. Sørensen, and O. Bang, "Nano-engineering of photonic crystal fibers for Supercontinuum generation," in *Photonic Crystals and Fibers*, W. Urbanczyk, B. Jaskorzynska, and P. St. J. Russell, eds., *Proc. SPIE* **5950**, 185–192 (2005).
- G. P. Agrawal, *Nonlinear Fiber Optics*, 3rd ed. (Academic, 2001).
- J. E. Sharping, M. Fiorentino, A. Coker, P. Kumar, and R. S. Windeler, "Four-wave mixing in microstructure fiber," *Opt. Lett.* **26**, 1048–1050 (2001).
- W. J. Wadsworth, N. Joly, J. C. Knight, T. A. Birks, F. Biancalana, and P. St. J. Russell, "Supercontinuum and four-wave mixing with Q-switched pulses in endlessly single-mode photonic crystal fibres," *Opt. Express* **12**, 299–309 (2004).
- W. Shuang-Chun, S. Wen-Hua, Z. Hua, F. Xi-Quan, Q. Lie-Jia, and F. Dian-Yuan, "Influence of higher-order dispersions and Raman delayed response on modulation instability in microstructured fibres," *Chin. Phys. Lett.* **20**, 852–854, doi:10.1088/0256-307X/20/6/321 (2003).
- K. J. Blow and D. Wood, "Theoretical description of transient stimulated Raman scattering in optical fibers," *IEEE J. Quantum Electron.* **25**, 2665–2673 (1989).
- S. Coen, D. A. Wardle, and J. D. Harvey, "Observation of non-phase-matched parametric amplification in resonant nonlinear optics," *Phys. Rev. Lett.* **89**, 273901/1-4, doi:10.1103/PhysRevLett.89.273901 (2002).
- F. Vanholsbeeck, P. Emplit, and S. Coen, "Complete experimental characterization of the influence of parametric four-wave mixing on stimulated Raman gain," *Opt. Lett.* **28**, 1960–1962 (2003).
- F. Biancalana, D. V. Skryabin, and P. St. J. Russell, "Four-wave mixing instabilities in photonic-crystal and tapered fibers," *Phys. Rev. E* **68**, 046603, doi:10.1103/PhysRevE.68.046603 (2003).
- J. Riishede, "Modelling photonic crystal fibres with the finite difference method," Ph.D. dissertation (Research Center COM, Technical University of Denmark, 2005).
- C. A. De Francisco, B. V. Borges, and M. A. Romero, "A semivectorial method for the modeling of photonic crystal fibers," *Microwave Opt. Technol. Lett.* **38**, 418–421 (2003).
- Overview of the BlazePhotonics nonlinear line, <http://www.crystal-fibre.com/products/nonlinear.shtml>(2005).
- O. V. Sinkin, R. Holzöhner, J. Zweck, and C. R. Menyuk, "Optimization of the split-step Fourier method in modeling optical-fiber communications systems," *J. Lightwave Technol.* **21**, 61–68 (2003).
- T. Schreiber, J. Limpert, H. Zellmer, A. Tünnermann, and K. P. Hansen, "High average power supercontinuum generation in photonic crystal fibers," *Opt. Commun.* **228**, 71–78, doi:10.1016/j.optcom.2003.09.091 (2003).
- K. P. Hansen, Crystal Fiber A/S (personal communication, 2006).